Letter

Nonlinear interference and electron dynamics: Probing photoelectron momentum distributions in strong-field ionization

Danish Furekh Dar* and Stephan Fritzsche

Helmholtz-Institut Jena, Fröbelstieg 3, D-07743 Jena, Germany;
GSI Helmholtzzentrum für Schwerionenforschung GmbH, Planckstrasse 1, D-64291 Darmstadt, Germany;
and Theoretisch-Physikalisches Institut, Friedrich-Schiller-Universität Jena, Max-Wien-Platz 1, D-07743 Jena, Germany

(Received 1 November 2023; accepted 29 February 2024; published 5 April 2024)

Nonlinear interference in the interaction of intense laser pulses with atoms profoundly affects the photoelectron momentum distribution (PMD). We theoretically show that the interference pattern in the PMD arises from the interaction of electrons with the fundamental frequencies concealed within the pulse. Nonlinear interference also imprints distinctive features on the ionization spectrum, providing valuable information about electron dynamics and phase relationships within the laser pulse. Additionally, the augmentation of optical cycles induces a distinct confinement in the PMD.

DOI: 10.1103/PhysRevA.109.L041101

Strong-field ionization is a crucial initial stage in many experiments that aim to uncover and manipulate the intricate dynamics of atoms, molecules, and solids [1,2]. Accurate interpretation of the outcomes of these experiments requires a deep understanding of nonlinear ionization dynamics in the presence of intense optical fields. The electrons ionized by a strong field can trigger a diverse range of dynamic processes in strong-field and attosecond physics [3,4].

Recent developments in high-intensity laser technology have enabled the generation and manipulation of pulses with just a few optical cycles [5,6]. Such pulses can be characterized by a vector potential of the form $\boldsymbol{A}(t) = \frac{A_0}{\sqrt{1+\epsilon^2}} f(t)[\cos(\omega_0 t + \phi_{\rm cep})\boldsymbol{e_x} + \epsilon\Lambda \sin(\omega_0 t + \phi_{\rm cep})\boldsymbol{e_y}]$, where A_0 represents the magnitude, $f(t)$ denotes the envelope, ω_0 signifies the frequency, $\phi_{\rm cep}$ refers to the carrier-envelope phase (CEP), and corresponding ellipticity and helicity are given by ϵ and Λ, respectively. On a significantly short temporal scale [7,8], these pulses possess the capability to study molecular and atomic dynamics. The ionization process induced by these pulses is exquisitely sensitive to the pulse shape and the CEP, highlighting the importance of precise control over these parameters [9–11].

Few-cycle pulses are the superposition of plane wave beams with slightly different phases [12]. Each plane wave contributes a specific phase and amplitude to the overall pulse by interfering constructively and destructively to create the desired temporal shape. This unique temporal structure has a profound impact on the photoelectron momentum distribution (PMD) in strong-field laser-matter interactions. The PMD, which describes the probability of finding electrons with various momenta, becomes highly sensitive to the precise characteristics of the few-cycle pulse, as seen from Fig. 1.

The strong-field approximation (SFA), also known as Keldysh-Faisal-Reiss (KFR) theory, is the most widely used analytical approach for describing the process of strong-field ionization of atoms, ions, and molecules [13–15]. There are various formulations of the SFA, but they all share the common notion that electron continuum states can be approximated by plane Volkov waves. These waves are exact solutions to the Schrödinger equation when a free electron interacts with a plane electromagnetic wave [16].

In this Letter, we report that nonlinear interference influences the PMD and ionization spectrum of atoms under intense laser pulses. Using the strong-field approximation, we demonstrate that these complex interference patterns arise from the electron's interaction with the laser pulse's fundamental frequencies, leaving distinctive marks on the ionization spectrum. An increase in optical cycles leads to PMD confinement perpendicular to the laser's propagation direction. This work offers insights into intense laser-atom interactions and electron dynamics, relevant to phenomena such as above-threshold ionization, recollision processes, high harmonic generation, and nonsequential double ionization [17–20].

We begin by considering the evolution of an electron from an initial hydrogenlike $1s$ state, defined by the wave function $|\Psi_0(t)\rangle$, to a continuum state $|\Psi_{\boldsymbol{p}}(t)\rangle$. In the SFA, the transition amplitude for such a direct electron ionization reads

$$T_{\boldsymbol{p}}^{(0)} = (-i)\int_0^{\tau_p} d\tau \langle \chi_{\boldsymbol{p}}(\tau)|\hat{V}_{\rm le}(\boldsymbol{r},\tau)|\Psi_0(\tau)\rangle. \qquad (1)$$

The laser field is activated at a certain starting time $t_0 = 0$, and its pulse duration is denoted by τ_p. We describe the electric field $E(\tau)$ emitted by the laser through a vector potential $\mathbf{A}(\tau)$, which satisfies the condition $\mathbf{A}(\tau) = 0$ for $\tau < 0$ and $\tau > \tau_p$. The continuum state is approximated by the Volkov state through the time evolution operator as $\langle \Psi_{\boldsymbol{p}}(t)|\,\hat{U}_{\rm le}(t,\tau) \approx \langle \chi_{\boldsymbol{p}}(\tau)|$. In the velocity gauge, the laser-electron interaction potential is given by $\hat{V}_{\rm le}(\boldsymbol{r},\tau) = \boldsymbol{A}(\tau)\cdot \boldsymbol{p} + \frac{1}{2}\boldsymbol{A}^2(\tau)$.

*danish.dar@uni-jena.de

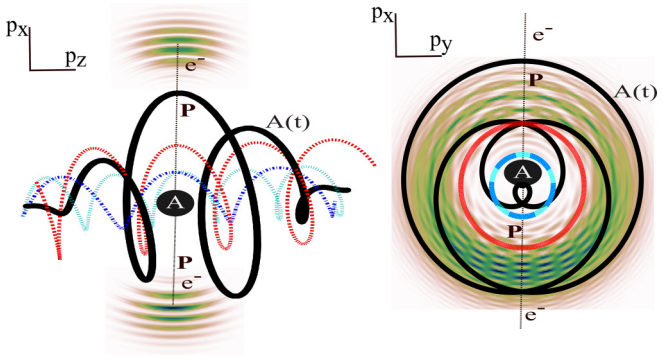

FIG. 1. Schematic representation of strong-field ionization. The left panel illustrates the momentum distribution of a photoelectron emitted from an atom (A) ionized by a strong laser pulse, with the colored lines indicating the frequencies within the pulse imprinted on the momentum distribution along the propagation direction. The right panel displays the momentum distribution of photoelectrons in the laser polarization direction. In both scenarios, the laser pulse is characterized by the vector potential $\mathbf{A}(t)$, depicted as the solid black line.

We now simplify the initial wave function to a hydrogenlike $1s$ state and substitute it with a modified ionization potential, denoted by I_p. The initial wave function can then be expressed as $|\Psi_0(t)\rangle = |\Psi_0\rangle\, e^{iI_p t} = \frac{2I_p^{\frac{3}{2}}}{\sqrt{\pi}} e^{-\sqrt{2I_p}\boldsymbol{r}} e^{iI_p t}$. So far, we have described the basic framework of the transition amplitude in the strong-field limit. We now turn our attention to the Volkov state, specifically focusing on the characteristics of the laser pulse. The Volkov state is a solution to the Schrödinger equation that comprises a plane wave component and a phase that describes the classical action of a free electron. In the velocity gauge, the Volkov state can be represented as $\chi_{\boldsymbol{p}}(\boldsymbol{r},\tau) = \frac{e^{-iS_v(\tau)}}{(2\pi)^{3/2}} e^{i\boldsymbol{p}\cdot\boldsymbol{r}}$, where $S_v(\tau) = \frac{1}{2}\int^{\tau} dt'[\boldsymbol{p} + \boldsymbol{A}(t')]^2$ denotes the Volkov phase.

To solve the Volkov states, we consider the vector potential of a circularly polarized laser pulse ($\epsilon = 1$) with an envelope described by a sine-squared function $f(t) = \sin^2(\omega_0 t/2n_p)$, for $0 \leqslant t \leqslant \tau_p$ and 0 otherwise, where n_p is the number of optical cycles. We can expand the trigonometric products and modify the vector potential as a superposition of three monochromatic plane-wave beams with different frequencies [12,21]:

$$\boldsymbol{A}(t) = \sum_{j=-1}^{1} \frac{A_j}{\sqrt{2}}[\cos(\omega_j t + \phi_{\rm CEP})\boldsymbol{e}_x + \Lambda \sin(\omega_j t + \phi_{\rm CEP})\boldsymbol{e}_y], \quad (2)$$

where j represents the indices for the lower (-1), central (0), and upper (1) frequencies. Specifically, when $j = -1$, the frequency ω_j is given by $\omega_j = (1 - 1/n_p)\omega_0$. For $j = 0$, the frequency ω_j equals ω_0, and for $j = 1$, the frequency is $\omega_j = (1 + 1/n_p)\omega_0$. The amplitude of the vector potential of each frequency also changes by $-A_0/4$, $A_0/2$, and $-A_0/4$ for the lower, central, and upper frequencies, respectively.

Figure 2 displays the vector potential (2) as a function of time as well as frequency by taking the Fourier transform. In the frequency domain, the superposition of just three

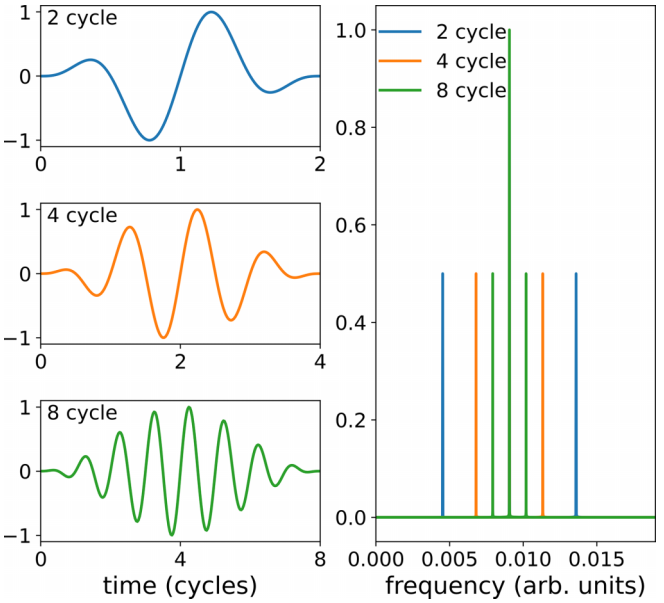

FIG. 2. Vector potential $\mathbf{A}(t)$ of a circularly polarized laser pulse as function of time (left panels) and frequency $[\mathcal{F}(\mathbf{A})](\omega)$ (right panel). This potential is shown for pulses with two (blue), four (orange) and eight (green) optical cycles, a carrier-envelope phase $\phi_{\rm cep} = 0$, and wavelength $\lambda = 800$ nm of the incident laser light. The ordinate in the right panel shows the absolute amplitude of the vector potential at a peak intensity of 5×10^{14} W/cm^2, and the amplitude provides insight into its contributions to the PMD in strong-field ionization measurements.

frequencies arises from the $\sin^2$ envelope of the pulse with finite duration. As seen from the right panel, this frequency spectrum can be modified by either adjusting the laser frequency ω_o or the number of optical cycles within the pulse. In strong-field ionization, both of these adjustments then also affect the PMD and may lead to either an enhanced or a suppressed yield of emitted photoelectrons.

To obtain the solution of the Volkov state, it is necessary to resolve the Volkov phase. The Volkov phase for a pulse with vector potential (2) can be written as

$$S_v(\tau) = \epsilon_p\,\tau + \frac{A_0^2}{4}\int^{\tau} dt' f^2(t') + \sum_{j=-1}^{1} \frac{A_j\, p\, \sin\theta_p}{\sqrt{2}} \int^{\tau} dt' \cos(\omega_j t' + \beta), \quad (3)$$

where, for the sake of brevity, we use $\beta = \phi_{\rm cep} - \Lambda\,\varphi_p$ and $\epsilon_p = \boldsymbol{p}^2/2$. θ_p and φ_p are the corresponding polar and azimuthal angles, respectively. The Volkov phase comprises again three terms: (i) the contribution due to the asymptotic energy ϵ_p of the photoelectron at the detector; (ii) the contribution due to its ponderomotive energy of the electron as accumulated within the envelope of laser pulse, and (iii) the contribution due to the momentum as obtained from its interaction with the frequency components of the laser pulse. Below, we refer to the second and third terms as the envelope energy and nonlinear response (terms), respectively.

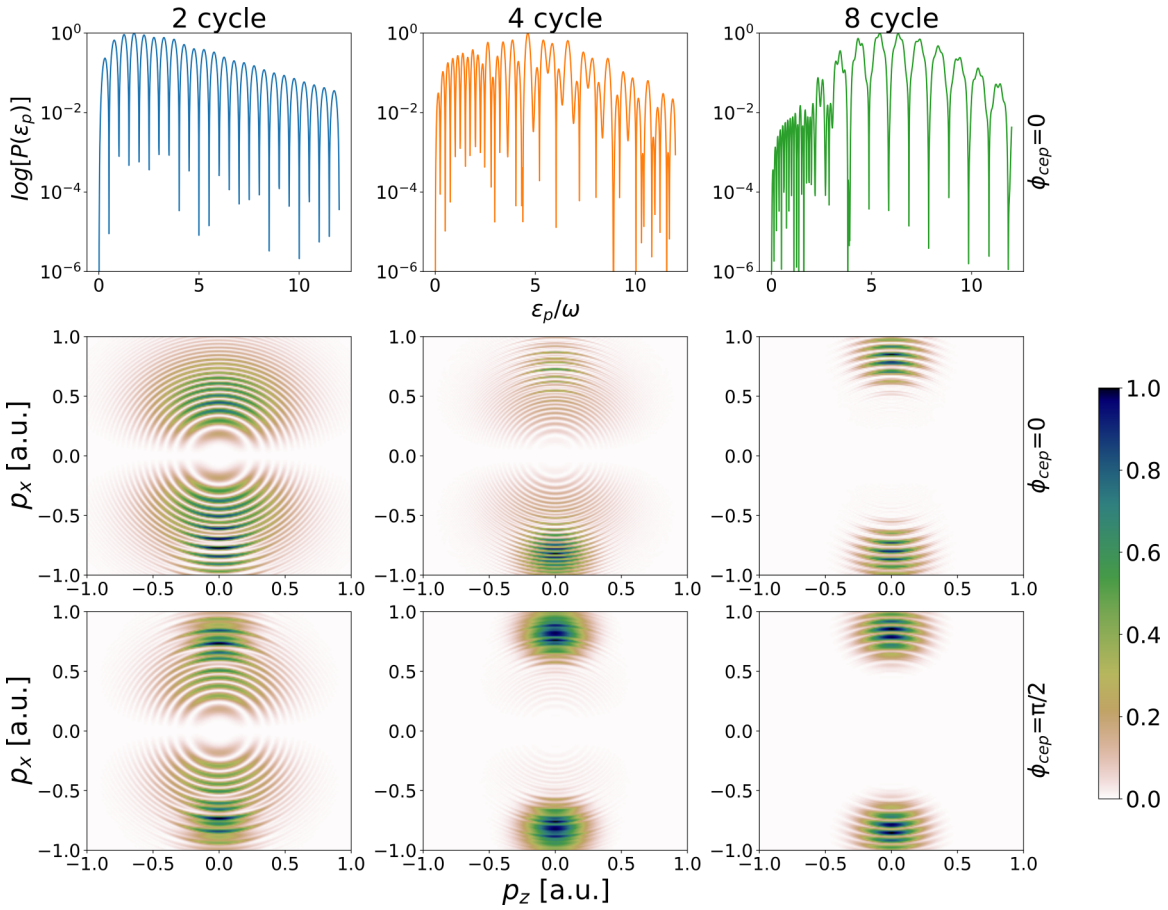

FIG. 3. ATI energy spectra and PMD for a $\sin^2$ driving laser laser pulses with two (left column), four (middle column), and eight optical cycles (right column). The ATI energy spectra (upper row) are shown as functions of ϵ_p(units of ω) and for $p_z = 0$, whereas the PMD are displayed in the p_x-p_z plane for the carrier-envelope phases $\phi_{\rm cep} = 0$ (middle row) and $\phi_{\rm cep} = \pi/2$ (lower row), respectively. All distributions are shown for a laser with wavelength $\lambda = 800$ nm and peak intensity $I = 5 \times 10^{14}$ W/cm^2 as well as for an argon target with ionization potential $I_p = 15.7596$ eV.

Using the vector potential (2), we calculate the PMD in strong-field ionization within the SFA. The photoionization probability [12] is given by

$$P(\boldsymbol{p}) = p\,|T_{\mathbf{p}}|^2 \;\approx\; p\,\left|T_{\mathbf{p}}^{(0)}\right|^2, \tag{4}$$

focusing on the direct transition amplitude (1). Figure 3 presents the energy and momentum distributions for laser pulses of two, four, and eight optical cycles. In the above-threshold ionization (ATI) spectra, each peak corresponds to a concentric ring in the PMD at $p_z = 0$, with the inner and outer rings indicating photoelectrons at the lowest and highest kinetic energies, respectively, often emitted at low probabilities. The distributions generally highlight photoelectrons with moderate kinetic energy.

As seen from the PMD in Fig. 3, the inner rings quickly dissolve as the number of pulse cycles increase, while the outer rings get broadened. Of course, the same lowering and broadening of peaks appear in the ATI spectra as n_p becomes larger. For an increasing number of cycles, however, new features arise in the ATI spectra. At the higher photoelectron energies, the peaks get broader with small oscillations on top of them. To explain these oscillations, we derive the Volkov state using the vector potential in Eq. (2). By using a Jacobi-Anger expansion to the Volkov phase, we can express the Volkov state as (see Supplemental Material [22] for detailed solution)

$$\chi_{\mathbf{p}}(\mathbf{r}, t) = (2\pi)^{-3/2} \prod_{i=1}^{5} \sum_{n_i=-\infty}^{\infty} J_{n_i}(x_i)\, e^{-i(E_N t - \boldsymbol{p}\cdot\boldsymbol{r} - \Phi_N)}. \tag{5}$$

In this expression, the summation index n_i counts the photons that are absorbed from the beam, whereas the arguments of the Bessel functions $x_1, \ldots, x_5$ have the values $U_p n_p/2\omega$, $U_p n_p/16\omega$, $\rho_0/2$, $-\rho_0/4(1 - 1/n_p)$, and $-\rho_0/4(1 + 1/n_p)$, respectively. Moreover, $\rho_0 = A_0\, p \sin\theta_p/\sqrt{2}\omega$ and U_p is the pondermotive energy.

The modified photoelectron energy (E_N) is given by $E_N = \frac{p^2}{2} + \frac{3U_p}{8} + [-n_1/n_p + 2n_2/n_p + n_3 + n_4(1 - 1/n_p) + n_5(1 + 1/n_p)]\omega$. Similarly, the modified phase (ϕ_N) is defined as $\phi_N = (n_3 + n_4 + n_5)(\phi_{\rm CEP} - \Lambda\varphi_p)$. It is now apparent that the set of n_i satisfies the equation $(\frac{-n_1+2n_2-n_4+n_5}{n_p} + n_3 + n_4 + n_5)\omega = N\omega$, where N is a fixed integer. This equation plays a crucial role in determining the final kinetic energy of the photoelectron. $N\omega$ specifies the energy of the absorbed photon, while n_i represents the fraction of photons absorbed at individual frequencies.

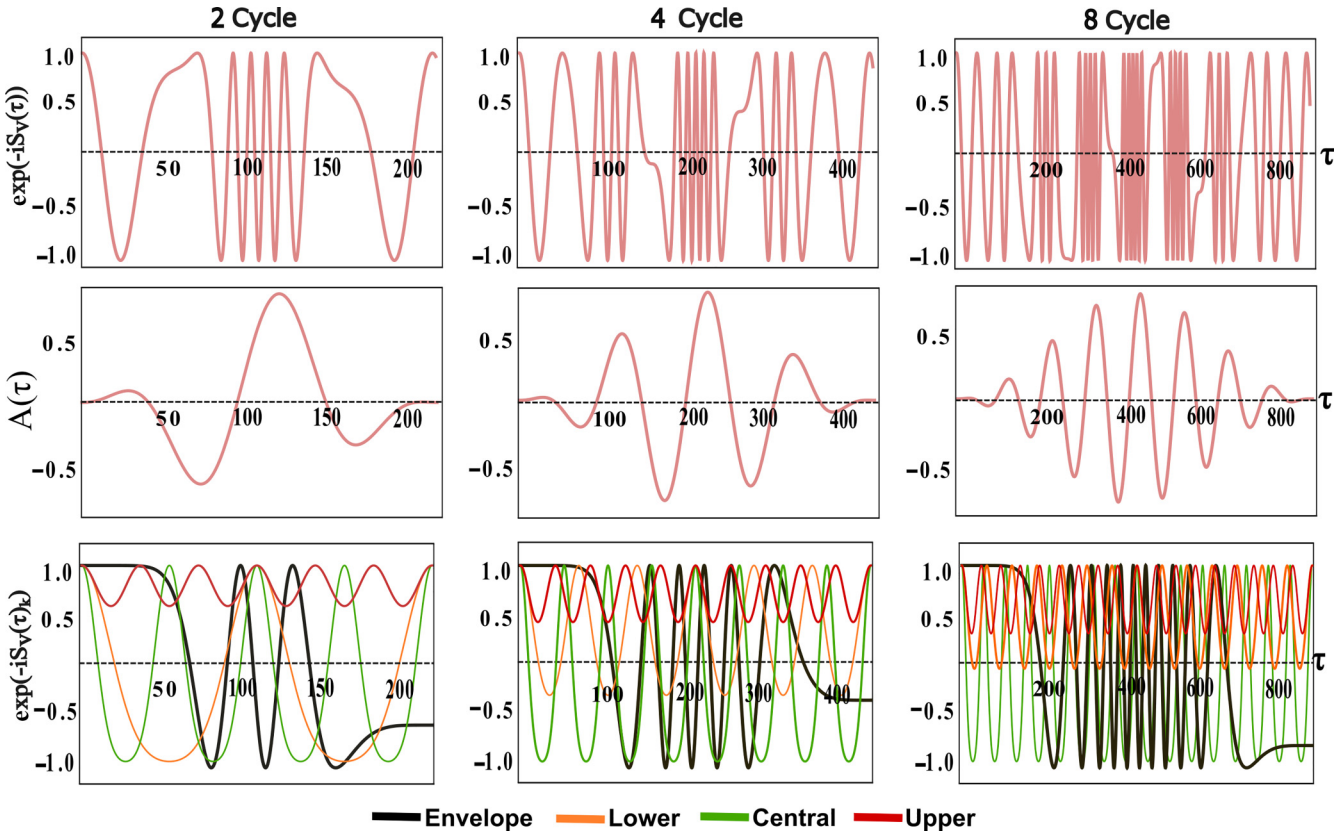

FIG. 4. Temporal evolution of the Volkov phase (3) at $p = 0.5$ a.u., including the full contribution (top row) and contributions from individual terms (bottom row), as derived from the analytical solution of the time-dependent Schrödinger equation (TDSE). $S_v(\tau)_k$ are the four terms in Eq. (3) representing the four components and only the real components of $S_v(\tau)_k$ and $S_v(\tau)$ are shown. Each panel sequence (from left to right) represents varying cycle counts (two, four, and eight), corresponding to a wavelength of 800 nm and an intensity of 5×10^{14} W/cm^2. β and θ_p are set to 0 and $\pi/2$, respectively. The profile of the vector potential is shown in arbitrary units (middle row).

The energy conservation for an ATI order N is given by

$$\epsilon_p = N\omega - \left(\frac{3U_p}{8} + I_p\right), \tag{6}$$

where I_p is the ionization potential. The cyclical peaks in the photoelectron spectrum, depicted in Fig. 3, result from the stepwise increase of N with energy, moderated by the Bessel functions' behavior in the Volkov state (5). These peaks, whose spacings reflect the photon energy, exhibit energy variations not strictly aligned with photon energy multiples, detailed in our Supplementary Material [22].

Equation (6) shows that the ponderomotive energy crucially influences ionization peak positioning due to oscillating electromagnetic fields. In few-cycle pulses, intense fluctuations create varying ponderomotive potentials across cycles, causing incoherent ionization amplitude alignment at different energy levels, affecting ATI peak formation. Ionization shifts towards lower energies near peak fields, and to higher energies at lower intensities, altering the photoelectron spectrum's ATI peaks.

Regarding the Bessel function parameters and their physical implications, x_1 and x_2 relate to pulse envelope energy, whereas $x_{3,4,5}$ correspond to the nonlinear response at different frequencies. The first two parameters change with the optical cycles in the pulse, while the latter three also depend on photoelectron momentum. Hence, envelope energy Bessel functions oscillate faster with longer pulses, and nonlinear response functions oscillate faster with increased photoelectron momentum. For pulses with fewer optical cycles, envelope energy oscillations dominate, minimizing interference, as shown in Fig. 3 for lower energies in four and eight-cycle cases. With more optical cycles, both envelope energy and nonlinear response enhance oscillations, leading to visible interference patterns in higher-energy ranges, as depicted in Fig. 3 for the same cases.

The interference patterns in photoelectron spectra, influenced by the temporal evolution of the Volkov phase (3), are crucial for understanding the photoelectron dynamics. As depicted in Fig. 4, the real part of the cumulative Volkov phase for varying pulse durations and the vector potential profile are analyzed at a photoelectron momentum of 0.5 a.u. and a laser wavelength of 800 nm. It is observed that the Volkov phase oscillates significantly at vector potential peaks, with oscillations intensifying with longer pulse durations. Detailed analysis of Fig. 4 (bottom row) reveals the role of the envelope energy and three distinct frequencies from the nonlinear photoelectron response. For short pulses (two-cycle case), distinct phase differences among these frequencies broaden the Volkov phase peaks. As pulse duration extends, these phase differences diminish, yet oscillations strengthen, leading to

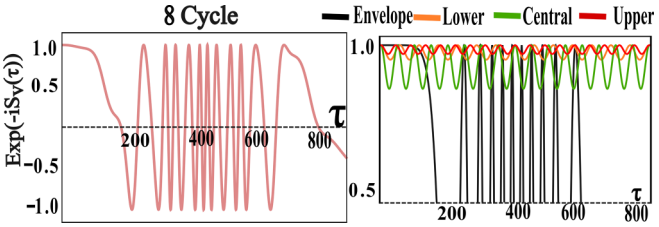

FIG. 5. Temporal evolution of a Volkov phase for an eight-cycle pulse. The left panel shows the composite effect of the temporal evolution of the Volkov phase within the laser pulse, while the right panel focuses on the contribution from the primary two terms. The laser parameters are the same as those in Fig. 4, except for the parameter p, which is set to 0.1 a.u.

interference effects that accelerate the Volkov phase oscillations. Conversely, at a lower photoelectron momentum of 0.1 a.u. (Fig. 5), the envelope energy predominantly drives the Volkov phase's temporal evolution. The amplitude variations across different components' envelopes, lower, upper, and central frequencies, highlight their collective contribution to the phase profile's reconstruction, as shown in the top row of Fig. 4.

To this end, we analyzed the interference patterns observed in PMD arising from the ionization by few-cycle pulses shaped with a $\sin^2$ envelope. This phenomenon is anticipated to be consistent across other trigonometrically based envelope functions, given their discrete spectral nature which facilitates decomposition into distinct frequency components. Contrarily, a Gaussian envelope, characterized by its continuous and extensive spectral distribution, is likely to induce interference features that diverge from those documented in our study. The wider frequency range of a Gaussian envelope can diminish the contrast of interference fringes, a consequence of the superposition over a continuous frequency spectrum. Moreover, Gaussian-type envelopes pose significant challenges for analytical solutions, rendering them beyond the analytical scope of our current study.

Increasing the number of optical cycles in a laser pulse not only affects nonlinear interference but also leads to a narrower electron emission, as evidenced by a decrease in the PMD width. This is illustrated in Fig. 6, where the full width at half maximum (FWHM) of the most intense ring in the momentum distribution narrows with more optical cycles. This effect is attributed to the enhanced ability of electrons to react to the laser's electric-field fluctuations during each optical cycle. Short pulses with fewer cycles produce a wider PMD due to limited interaction time, whereas longer pulses with more cycles allow electrons to more precisely follow the laser field's variations, resulting in a more focused PMD around certain polar angles within each cycle.

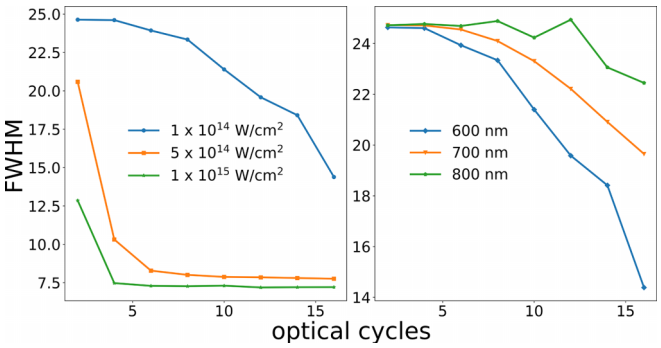

FIG. 6. Full width at half maximum (FWHM) of the prominent ring with the highest intensity in the momentum distribution within the propagation plane. The lines in the figure demonstrate a trend: at higher optical cycles, the FWHM progressively decreases for increasing intensity and vice versa for wavelength. (Left) The wavelength remains consistent at 600 nm. (Right) The intensity remains consistent at $1 \times 10^{14}\,\mathrm{W/cm^2}$.

In summary, we report the observation of intricate nonlinear interference in strong-field ionization. Such interference has a profound impact on the photoelectron momentum distribution and the ionization spectrum. By utilizing the strong-field approximation, we showed that these nonlinear interference patterns in the PMD originate from the interaction of electrons with individual frequencies concealed within the laser pulse. Furthermore, we emphasize that nonlinear interference imparts unique characteristics to the ionization spectrum, providing valuable insights into the behavior of electrons and the phase relationships inherent in the laser pulse. Additionally, our research highlights that increasing the number of optical cycles in the laser pulse induces a distinct confinement effect within the PMD. These findings significantly enhance our comprehension of intense laser field interactions, rendering them a potent tool for exploring complex electron dynamics. Notably, these insights hold relevance for phenomena such as above-threshold ionization, recollision processes, high harmonic generation, and nonsequential double ionization.

This research has received funding from the Research School of Advanced Photon Science (RS-APS) at the Helmholtz Institute Jena, Germany. We extend our sincere appreciation for the access to the "Draco" High Performance Computing (HPC) cluster at Friedrich Schiller University Jena, which played a crucial role in facilitating the computational aspects of our research. We are grateful to Professor Dr. Gerhard G. Paulus for his helpful discussions and feedback on this research.

[1] P. B. Corkum and F. Krausz, Attosecond science, Nat. Phys. **3**, 381 (2007).

[2] B. Sheehy and L. F. DiMauro, Atomic and molecular dynamics in intense optical fields, Annu. Rev. Phys. Chem. **47**, 463 (1996).

[3] F. Krausz and M. Ivanov, Attosecond physics, Rev. Mod. Phys. **81**, 163 (2009).

[4] P. H. Bucksbaum, M. Bashkansky, and D. W. Schumacher, Above-threshold ionization in helium, Phys. Rev. A **37**, 3615 (1988).

[5] T. Brabec and F. Krausz, Intense few-cycle laser fields: Frontiers of nonlinear optics, Rev. Mod. Phys. **72**, 545 (2000).

[6] M. Nisoli, S. D. Silvestri, O. Svelto, R. Szipöcs, K. Ferencz, C. Spielmann, S. Sartania, and F. Krausz, Compression of high-energy laser pulses below 5 fs, Opt. Lett. **22**, 522 (1997).

[7] A. H. Zewail, Femtochemistry: Recent progress in studies of dynamics and control of reactions and their transition states, J. Phys. Chem. **100**, 12701 (1996).

[8] P. H. Bucksbaum, Ultrafast control, Nature (London) **421**, 593 (2003).

[9] C. P. J. Martiny and L. B. Madsen, Symmetry of carrier-envelope phase difference effects in strong-field, few-cycle ionization of atoms and molecules, Phys. Rev. Lett. **97**, 093001 (2006).

[10] D. Chetty, R. D. Glover, X. M. Tong, B. A. deHarak, H. Xu, N. Haram, K. Bartschat, A. J. Palmer, A. N. Luiten, P. S. Light, I. V. Litvinyuk, and R. T. Sang, Carrier-envelope phase-dependent strong-field excitation, Phys. Rev. Lett. **128**, 173201 (2022).

[11] S. Li, B. Jochim, J. Stamm, D. Peng, H.-C. Shao, J. M. Ngoko Djiokap, and M. Dantus, Pulse shaping in strong-field ionization: Theory and experiments, Phys. Rev. A **105**, 053105 (2022).

[12] D. B. Milošević, G. G. Paulus, D. Bauer, and W. Becker, Above-threshold ionization by few-cycle pulses, J. Phys. B: At., Mol. Opt. Phys. **39**, R203 (2006).

[13] L. V. Keldysh, Ionization in the field of a strong electromagnetic wave, Sov. Phys. JETP **20**, 1307 (1964).

[14] F. H. M. Faisal, Multiple absorption of laser photons by atoms, J. Phys. B: At., Mol. Opt. Phys. **6**, L89 (1973).

[15] H. R. Reiss, Effect of an intense electromagnetic field on a weakly bound system, Phys. Rev. A **22**, 1786 (1980).

[16] D. M. Wolkow, Über eine Klasse von Lösungen der Diracschen Gleichung, Z. Phys. **94**, 250 (1935).

[17] B. Böning and S. Fritzsche, Above-threshold ionization driven by Gaussian laser beams: Beyond the electric dipole approximation, J. Phys. B: At., Mol. Opt. Phys. **54**, 144002 (2021).

[18] F. Liu, S. Li, Z. Chen, B. Böning, and S. Fritzsche, Nonsequential double ionization of Ne with elliptically polarized laser pulses, Phys. Rev. A **106**, 043120 (2022).

[19] B. Minneker, B. Böning, and S. Fritzsche, Generalized nondipole strong-field approximation of high-order harmonic generation, Phys. Rev. A **106**, 053109 (2022).

[20] B. Yang, K. J. Schafer, B. Walker, K. C. Kulander, P. Agostini, and L. F. DiMauro, Intensity-dependent scattering rings in high order above-threshold ionization, Phys. Rev. Lett. **71**, 3770 (1993).

[21] D. F. Dar, B. Minneker, and S. Fritzsche, Nondipole strong-field approximation for above-threshold ionization in a few-cycle pulse, Phys. Rev. A **107**, 053102 (2023).

[22] See Supplemental Material at http://link.aps.org/supplemental/10.1103/PhysRevA.109.L041101 for a detailed solution to derive Eq. (5) and an in-depth analysis of the peak separation of the ionization peaks as presented in Figure 3 of the main manuscript.